The wind farm pressure field

Ronald B. Smith

Earth and Planetary Science Department, Yale University, New Haven, CT, 06520, USA

WES-2023-56 | Research article

Revision Date: August 16, 2023; Second Revision: October 21, 2023

Correspondence to: Ronald B. Smith

Email: ronald.smith@yale.edu

20   **Abstract** The disturbed atmospheric pressure near a wind farm arises from the turbine drag forces in combination with vertical confinement associated with atmospheric stability. These pressure gradients slow the wind upstream, deflect the air laterally, weaken the flow deceleration over the farm and modify the farm wake recovery. Here, we describe the airflow and pressure disturbance near a wind farm under typical stability conditions and alternatively, with the simplifying assumption of a rigid lid. The rigid lid case clarifies the cause of the pressure disturbance and its close relationship to wind farm drag.

25   The key to understanding the rigid lid model is the proof that the pressure field p(x,y) is a Harmonic Function almost everywhere. It follows that the maximum and minimum pressure occur at the front and back edge of the farm. Over the farm, the favorable pressure gradient is constant and significantly offsets the turbine drag. Upwind and downwind of the farm, the pressure field is a dipole given by $p(x,y) \approx Axr^{-2}$ where the coefficient A is proportional to the total farm drag. Two derivations of this law are given. Field measurements of pressure can be used to find the coefficient A and thus to estimate

30   total farm drag.

1. Introduction

35   The construction of offshore wind farms may significantly help our society transition to renewable energy but the wind slowing by these farms may ultimately limit their potential for electric power generation (Ahktar et al. 2022). This issue has an extensive literature, reviewed recently by Stevens and Meneveau (2017), Archer et al. (2018), Porte-Agel et al. (2020), Pryor et al. (2020), Fischereit et al. (2021). An integral part of the wind slowing by turbine drag is the creation of a local pressure field. This pressure disturbance was initially neglected (Jensen 1983) but has been recently estimated in connection with gravity

40   wave (GW) generation (Smith 2010, 2022, Wu and Porté-Agel, 2017, Allaerts and Meyers, 2018, 2019). In a stably stratified atmosphere, the lifting of the air caused by farm drag creates gravity waves aloft whose pressure field acts back on the lower atmosphere.

This pressure field modifies the airflow in ways that the direct action of turbine drag cannot. First, it can decelerate the flow before it reaches the first row of turbines, so called "blockage" (Bleeg et al. 2018) in wind farm terminology or "blocking" in

45   mountain meteorology. Second, it can deflect the air to the left and right. Third, over the farm, it can fight back against the turbine drag, helping to keep the wind flow strong. Finally, it slows the downwind recovery of the wake.

The pressure field near a wind farm is analogous in some respects to that for a single turbine. The airflow approaching a turbine disk begins to decelerate upwind due to an adverse pressure gradient and its corresponding "axial induction factor" reduces the turbine efficiency to the Betz limit (Hanson, 2000). According to Gribben and Hawkes (2019), the local non-hydrostatic

50   pressure disturbance decays inversely as the square of the distance upstream. The farm-generated hydrostatic pressure disturbance may be more far-reaching.

In discussing the cause of the pressure field, we shall exercise caution as the cause may be model dependent. In compressible subsonic aerodynamics, acoustic waves play a role in creating the pressure field. In stratified flow, gravity waves play a role. In presumed non-divergent flow, the pressure field is usually determined "diagnostically" as the cause is hidden from view.

55   The pressure field exists simply to keep the flow non-divergent.

In this paper, we compare the wind farm pressure field in the realistic gravity wave (GW) model with the idealized rigid lid (RL) model. The rigid lid approximation retains some of the features of the atmospheric problem but allows us to derive simple theorems and closed form solutions that clarify the cause, properties and impact of the pressure field.

We begin by recalling the governing equations for the two-layer model of Smith (2010) and describe the rigid lid (RL) limit.

60   Second, we derive approximate closed form expressions for the far-field and near-field pressure. Third, we discuss the cause of the pressure field and its role in the wind farm disturbance. Finally, we consider using pressure measurements to estimate total farm drag and the use of the RL model in industrial applications.

65.   The Gravity Wave (GW) model and the Rigid Lid (RL) limit

Our method for computing the response to wind farm drag forces uses a 2-layer stratified hydrostatic Gravity Wave (GW) model solved with Fast Fourier Transforms (FFT). This model consists of a lower "turbine layer" from which momentum is removed by specified drag forces and a Rayleigh restoring force that decays the farm wake (Smith 2010, 2022). An overlying density-stratified layer responds to vertical displacement and creates a hydrostatic pressure field $p(x, y)$ that acts back on the turbine layer. The linearized governing momentum equations for the turbine layer are

$$U \left(\frac{\partial u}{dx} \right) + V \left(\frac{\partial u}{\partial y} \right) = -\rho^{-1} \left(\frac{\partial p}{\partial x} \right) + F_x - Cu \tag{1a}$$

$$U \left(\frac{\partial v}{\partial x} \right) + V \left(\frac{\partial v}{\partial y} \right) = -\rho^{-1} \left(\frac{\partial p}{\partial y} \right) + F_y - Cv \tag{1b}$$

where $\vec{F}(x, y)$ is the turbine drag, $\vec{U}$ is the ambient wind, $\vec{u}(x, y)$ is the drag-induced wind perturbation wind and C is the Rayleigh restoring coefficient (Smith 2022). After these equations are solved for the perturbation wind field, the linearized scalar wind deficit is computed from $Deficit(x, y) = -(\vec{U} \cdot \vec{u})/|\vec{U}|$. Its area integral is the Total Deficit

$$TD = \iint Deficit(x, y) \, dxdy \tag{2}$$

Taking the dot product of (1) with the ambient wind $\vec{U} = (U, V)$ and integrating over the whole domain relates TD to the turbine drag (Smith 2022)

$$TD = \frac{-1}{|\vec{U}|C} \iint \vec{U} \cdot \vec{F}(x, y) \, dxdy \tag{3}$$

Because the pressure field $p(x, y)$ decays at infinity, it does not influence TD but alters the spatial distribution of $Deficit(x, y)$. The impact of the $Deficit$ on farm power generation is described by $\gamma = \overline{Deficit}/|\vec{U}|$, the normalized average $Deficit$ over the farm area. For example, $\gamma = 0.02$ is a 2% reduction in wind speed over the farm.

The GW model discussed herein uses the hydrostatic assumption and thus does not take into account the pressure field associated with vertical fluid acceleration. Pressure fields in this model are generated only by density anomalies aloft. If an airflow streamline approaching a wind farm curves sharply upwards, a region of non-hydrostatic high pressure will be generated below it. These effects are easily incorporated in the linearized FFT modeling framework, but we don't do that here. In mountain wave theory for example, such effects are usually neglected for horizontal scales greater than one kilometer. Non-hydrostatic effects are certainly important on the scale of an individual turbine but less so on the farm scale. However, some wind farm models, such as that of Gribben and Hawkes (2019), include this effect.

We first ran the two-layer GW model with the "realistic" parameters shown in Table 1. The model's two stability parameters are the reduced gravity g' of the inversion and Brunt-Vaisala frequency N of the troposphere given by

95
$$g' = g \frac{\Delta\theta}{\theta} = 0.1 \; ms^{-2} \;\; \text{and} \;\; N = \sqrt{\frac{g}{\theta}\frac{d\theta}{dz}} = 0.01 \; s^{-1} \tag{4}$$

where θ is the potential temperature. We set the Rayleigh restoring coefficient C to a fairly small value so the wake recovery

is slow, but fast enough to prevent periodic wrapping from the FFT method. To compute the turbine drag force $\vec{F}$, we define

the Disk Area Ratio (DAR) as the ratio of rotor disk area to planform farm area. We chose DAR=0.0077 and a turbine thrust

coefficient of $C_T = 0.75$. With a wind speed of $U = 10 ms^{-1}$ and turbine layer depth of H=400m, the wind farm drag per

100 unit air mass is then

$$|\vec{F}| = F = \frac{DAR*C_T*U^2}{2H} = \frac{(0.0077)(0.75)(10^2)}{2(400)} = 0.0007218 \; ms^{-2} \tag{5}$$

For illustration, we chose horizontal farm dimensions $a = b = 7000m$. The total drag on the farm is then

$$Drag = \rho \cdot a \cdot b \cdot H \cdot F \approx 17 \cdot 10^6 \; Newtons \tag{6}$$

A few output parameters from this reference run are given in Table 2, including the maximum vertical displacement of the

105 inversion, the maximum wind speed deficit, the normalized farm-averaged speed deficit (γ) and the difference between the

two pressure extrema (Δp) . In the reference run, the inversion is displaced upward by 11.8 meters, the maximum deficit is

$0.468 \; ms^{-1}$, the average relative deficit is $\gamma = 0.0315$ and there is a $\Delta p = 2.38$ Pascal pressure difference across the farm.

To investigate the influence of atmospheric stability (4), we ran the GW model several more times, first with the two stability

parameters $g' = N = 0$. When there is no stability, the turbine drag slows the airstream and displaces the top of the turbine

110 layer upwards, but no hydrostatic pressure disturbance is generated.

We then increased each stability parameter (4) from zero towards a large value (Table 2). The vertical displacement of the

fluid decreased towards zero and the pressure perturbations increased from zero. Other model output values changed only

slightly. The maximum wind speed deficit decreased slightly from $0.445 ms^{-1} \; to \; 0.323 ms^{-1}$ in the rigid lid limit. The

average relative speed deficit over the farm decreased slightly from $\gamma = 0.0226 \; to \; 0.0195$.

115 One striking aspect of Table 2 is that the g' series and the N series of runs approach the same "rigid lid" (RL) limit. The trends

are smooth for the N series but the g' series of runs shows a singularity when the Froude Number $Fr = U/\sqrt{g'H} \approx 1$.

Ultimately, increasing either type of stability takes us to the same rigid lid solution with finite wind deficit and pressure

difference but a vanishing vertical displacement. When $N = 0$, the vertical displacement approaches zero as $1/g'$ and when

$g' = 0$ it approaches zero as $1/N$.

120 The planform patterns of the gravity wave (GW) and rigid lid (RL) solutions are compared in Figures 1 and 2. The wind speed

deficit patterns (Figs 1a, 2a) show the wake caused by the farm drag but also show the influence of the pressure fields. Both

show upstream deceleration, stronger in the RL case, and lateral regions of accelerated flow downwind of the farm. The wind

speed deficit patterns over the farm are different also due to pressure forces acting on the flow. The pressure fields (Figs 1b,2b)

show an upwind maxima and downwind minima of approximately similar magnitude. The RL case however has these two extrema shifted upwind and the whole field is exactly anti-symmetric with respect to the upwind-downwind direction.

3. The Harmonic Pressure Field

We can understand the rigid lid (RL) solution more fully by noting that the pressure field $p(x, y)$ in that case is a Harmonic function almost everywhere. A Harmonic function is one which satisfies Laplace's Equation $\nabla^2 p = 0$. To prove this hypothesis, we apply the divergence operator to (1) giving

$$U(u_x + v_y)_x + V(u_x + v_y)_y = -\rho^{-1}(p_{xx} + p_{yy}) + F_{x,x} + F_{y,y} - C(u_x + v_y)$$

or
$$\vec{U} \cdot \nabla(\nabla \cdot \vec{u}) = -\rho^{-1} \nabla^2 p + \nabla \cdot \vec{F} - C(\nabla \cdot \vec{u}) \tag{7}$$

With the rigid lid, the horizontal flow field is non-divergent flow so $\nabla \cdot \vec{u} = 0$ and (7) becomes

$$\nabla^2 p = \rho \nabla \cdot \vec{F} \tag{8}$$

Thus, the RL pressure field is a Harmonic function except at the windward and leeward edges of the wind farm where the turbine drag force is divergent $(i.e. \nabla \cdot \vec{F} \neq 0)$.

To illustrate the Harmonic property of $p(x, y)$ we show the Laplacian of the pressure field for the reference GW case in Fig. 3a and the Rigid Lid case in Fig. 3b. They differ in important details. In Fig. 3a, $\nabla^2 p = 0$ is violated over most of the field in a complicated pattern while in Fig. 3b it is violated only over the farm front and back edges, in agreement with (8). The Laplacian in Figs 3 was computed in Fourier space with $\hat{\Delta}(k, l) = -(k^2 \hat{p}(k, l) + l^2 \hat{p}(k, l))$ and then inverted.

Recall that a harmonic function has no local maxima or minima and therefore only takes on values that are between the boundary values. As p(x,y) decays at infinity, the pressure would therefore vanish were it not for these two small non-Harmonic regions. Thus, these two regions in Fig 3b, "support" or "cause" the pressure field seen in Fig 2b.

4. The cause of the RL pressure field

In non-divergent flow, the role of pressure is to maintain the non-divergent property of the flow. As the turbine force field $\vec{F}(x, y)$ is divergent at the farm edges, the pressure field must arise instantly to prevent any flow divergence there. That is the meaning of (8). At the windward edge for example, the outward diverging pressure forces from the local high pressure balance the converging turbine drag forces.

This interpretation is supported by noting that pressure is insensitive to the Rayleigh restoring force coefficient C in (1). The dashed curve in Fig 4b, shows the wind speed deficit where we increase the coefficient tenfold to $C = 0.0033 \ s^{-1}$. In Fig. 4b, the wind speed deficit is dramatically reduced while the pressure field is unchanged. This independence of the pressure field from C is a unique feature of the Rigid Lid case and not found in the more general GW case where the Rayleigh force is

155 divergent. The Rayleigh force is non-divergent because the RL flow is non-divergent, and therefore it does not influence the pressure field.

5. Role of the pressure field

160 The two pressure fields, GW and RL, are compared along the centerline in Figs. 4a,b. Both transects have an upwind maximum and downwind minimum. The GW pressure field (Fig 4a) is smoother with a maximum over the farm and a smaller minimum in the near wake. In the rigid lid case (Fig 4b), the pressure maximum and minimum points are equal in magnitude and shifted upstream slightly to the farm edges. In both cases, the air decelerates as it approaches the farm under the adverse pressure gradient. The linearized Bernoulli equation derived from (1), $Uu(x) = -\rho^{-1}p(x)$ is approximately valid upwind,

165 so as the pressure rises the wind speed drops. There is also an adverse pressure gradient downwind of the farm. Overall, the pressure field smooths out the velocity field by spreading the deceleration up and down wind.

A key feature of the rigid lid solution is the linear pressure field over the farm, so we define

$$\Delta p = Max(p) - Min(p) \tag{9}$$

so the pressure gradient force is $\quad PGF = -\rho^{-1}\left(\dfrac{dp}{dx}\right) \approx \Delta p/\rho a \tag{10}$

170 Using values from Tables 1 and 2, the non-dimensional force ratio is

$$\frac{PGF}{F} = \frac{(3.18Pa)}{(1.2kg{\cdot}m^{-3})(7000m)(-0.0007218ms^{-2})} = -0.52 \tag{11}$$

Thus, in this case, the favorable pressure gradient cancels 52% of the turbine drag over the farm. The magnitude of this ratio increases with aspect ratio $AR = b/a$.

175

6. The far-field pressure

Equation (8) is the Poisson Equation where the scalar $\rho\nabla \cdot \vec{F}$ is the equivalent of a "point charge" in an electrostatic analogy. If we define $B(x,y) = \rho\nabla \cdot \vec{F}$ then the general solution to (8) using a Green's function is

$$p(x,y) = \left(\tfrac{1}{4\pi}\right) \iint \ln((x - x')^2 + (y - y')^2) \cdot B(x',y') \, dx'dy' \tag{12}$$

180 While the logarithm function in (12) diverges at infinity, (12) itself is well behaved because $\iint B dx dy = 0$. If we lump the front and back edge contributions into two delta functions,

$$B(x,y) \approx \rho Fb(\delta\left(x + \tfrac{a}{2}, y\right) - \delta\left(x - \tfrac{a}{2}, y\right)) \tag{13}$$

then from (12) for $r \gg a$, we obtain asymptotically the dipole

$$p(x,y) \approx \frac{-\rho Fabx}{2\pi r^2} = -A[\frac{x}{r^2}] \qquad (14a)$$

where $r = \sqrt{x^2 + y^2}$ and the constant

$$A = \left(\frac{1}{2\pi}\right)\rho \cdot F \cdot a \cdot b \qquad (14b)$$

This dipole formula (14) is consistent with the pressure field pictured in Fig 2b. The isobars for (14a) are circles touching each other at the origin. Thus, (14a) satisfies $p(x,0) = p(x/2, \pm x/2))$. On the 45 degree lines $(y = \pm x)$, $\partial p/\partial x = 0$; so the isobars are parallel to the x-axis there.

In the present computation (Table 1), the drag force is $F = 0.0007218\ ms^{-2}$ so we predict from (14b) that $A = 6754 Pa \cdot m$. We checked this prediction against our computed pressure field (Fig 3) by using the pressure at distance $d = 8km$ upstream from the farm center. Using (14a)

$$A = p(x = -d, y = 0)(d) = 6689 Pa \cdot m \qquad (15)$$

(see Table 2). The small 1% difference between these two A values verifies our solution. The 1% difference arises from the fact that 8km is not far enough upstream to be in the "far field".

The Green's Function method with two delta-functions (12,13) can also be used to find the pressure field near the farm center. The result is

$$p(x,y) \approx -2\ \frac{\rho Fbx}{a\pi} \qquad (16)$$

The non-dimensional force ratio for a=b is then

$$\frac{PGF}{F} \approx -\frac{2}{\pi} \approx -0.64 \qquad (17)$$

roughly similar to the computed FFT value in (11).

7. Alternate derivation of the drag induced pressure dipole

In the previous section, we used a Green's function solution to (8) to derive the far-field pressure dipole (14). We now re-derive this formula using a physical volume-conservation argument. When the farm drag slows the flow, it creates a volume flow deficit (Q) in the wake. A farm with downwind dimension "a" with drag force (F) per unit mass (units ms^{-2}) will create (from 1) a wake with speed deficit $Deficit = F \cdot a/U$. The lost volume flux in the wake is

$$Q = Deficit \cdot b \cdot H = F \cdot a \cdot b \cdot H/U \qquad (18a)$$

or using (6)
$$Q = \frac{Drag}{\rho U} \qquad (18b)$$

with units $m^3 s^{-1}$. We balance the volume budget by adding an equal point source Q at the origin. Confined to a layer of depth H, the velocity field from a point volume source Q is

$$u = \left(\frac{Q}{2\pi H}\right)\left(\frac{x}{r^2}\right) \text{ and } v = \left(\frac{Q}{2\pi H}\right)\left(\frac{y}{r^2}\right) . \tag{19}$$

215   The radial speed is $u_r = \sqrt{u^2 + v^2}$ so the volume flow is $Q = 2\pi r H u_r$.

If the mean flow U is added to the source flow (19), the total fluid speed at each point is

$$S^2 = (U + u)^2 + (v)^2 . \tag{20}$$

This combined flow is equivalent to the familiar Rankine Half-body of width $W = \frac{Fab}{U^2}$. A similar approach was used by Gribben and Hawkes (2019) for a single turbine.   In the absence of dissipation, Bernoulli's equation gives the pressure

220   anomaly at each point

$$p(x,y) = -\left(\frac{1}{2}\right)\rho(S^2 - U^2) \tag{21}$$

Combining (20,21) and linearizing gives a dipole pressure pattern in the far-field

$$p(x,y) \approx -\rho U\left(\frac{Q}{2\pi H}\right)\left(\frac{x}{r^2}\right) = -A(x/r^2) \tag{22}$$

where

225

$$A = \left(\frac{1}{2\pi}\right)\rho \cdot F \cdot a \cdot b \tag{23}$$

in agreement with (14).   If the total farm drag has been computed in Newtons, then using (6) the pressure coefficient is

$$A = \left(\frac{1}{2\pi H}\right)Drag \tag{24}$$

230   where H is the depth of the layer into which the drag has been applied. The pressure coefficient A has units $Pa \cdot m$.   If the farm is not rectangular, the product $a \cdot b$ in (23) can be replaced with the farm area.

8.   Blockage and Deflection

As the RL source function expression (19) provides good estimates of the far field pressure, we can use it to estimate airflow

235   blockage and deflection. For upstream blocking, the wind disturbance will decay inversely with distance upwind. At the front edge of the farm, we evaluate (19) to give

$$u\left(x = -\frac{a}{2}, y = 0\right) = \left(\frac{F \cdot a \cdot b}{2\pi U}\right)\left(\frac{x}{r^2}\right) = -\frac{F \cdot b}{\pi U} \tag{25}$$

The small pressure reduction and wind speed maxima near the downwind farm corners (Fig 1) can also be explained with these

240   formulae (22,25).

The upwind pressure field deflects the airflow to the left and right. The maximum lateral speed is located near the farm edge at $x = 0, y = b/2$. From (19),

$$v\left(x = 0, y = \frac{b}{2}\right) = \left(\frac{F \cdot a \cdot b}{2\pi U}\right)\left(\frac{y}{r^2}\right) = \frac{F \cdot a}{\pi U} \tag{26}$$

In the present example with a=b (Table 1), the magnitudes of u and v are both $0.16 ms^{-1}$. Potential errors in (25, 26) come from using the far field formulae too close to the farm and the influence of Rayleigh friction.

9. Application to "industrial" RL models

In addition to the conceptual value of the RL model emphasized herein, it could also be used in "industrial" or "engineering" models of wind farm disturbance. Any quasi-analytic model or Computational Fluid Dynamics (CFD) model could utilize the RL assumption to simplify the computation. This application of the rigid lid assumption could be justified by its easy incorporation atmospheric stability effects. Our results confirm this logic but only in a qualitative way. We have shown that the RL model over-idealizes the dipole and shifts the pressure field slightly upwind. Worse still would be the assumption that RL models will not have a pressure field because they do not support gravity waves. In fact, the rigid lid assumption requires that a pressure field be generated from the leading and trailing edge of the farm where the turbine drag vector field is divergent. ==A properly designed RL model would have a dipole pressure field very similar to that described in (14) and (22).==

10. Determining total farm drag from pressure measurement

The direct link between farm drag and far-field pressure dipole (14, 24) in the RL case allows us to determine total farm drag with a pair of pressure measurements. If pressure sensors are located a distance "d" upwind and downwind of the farm center, then the difference in pressure between those two sensors ΔP_M gives the pressure dipole coefficient using (14 or 22)

$$A = \Delta P_M \cdot d/2 \tag{27}$$

From A, the total farm drag is found using (24)

$$Drag = 2\pi HA \tag{28}$$

In the rigid lid case (Fig 3b) the pressure values 8km upstream and downstream are $p = \pm 0.84 Pa$ so $\Delta P_M = 1.68 Pa$. Using (27,28), we obtain $A = 6720\ Pa \cdot m$ and the total farm drag is $Drag \approx 17 \times 10^6 Nt$ in agreement with the specified drag in Table 1.

In the reference GW case (Fig 3a), the upstream and downstream pressure values are $p = 0.292 Pa$ and $p = -0.607 Pa$ so $\Delta P_M = 0.899 Pa$. Using these GW case values in the rigid lid formulae (27,28) gives $Drag \approx 9 \times 10^6 Nt$. Thus, the error in (27, 28) is large, but a measured ΔP_M still provides a useful lower bound on the farm drag. If more accuracy is needed, use the linear GW model or a full-physics mesoscale model.

11. Discussion

When turbine drag in a wind farm slows the wind, the lowest layer must thicken to conserve mass and push the higher layers upwards. The influence of this lifting depends on the atmospheric static stability. With no stratification, this upward displacement will not generate a hydrostatic pressure disturbance.

When moderate stable stratification is present, the upward displacement will create pressure anomalies that act on the turbine layer. The computation of the pressure field typically requires the use of a gravity wave (GW) model. When the stratification is very strong, the GW solutions approach the rigid lid (RL) limit where little or no vertical displacement occurs. In this situation, we can compute the pressure field directly from the non-divergent assumption, without having to consider gravity waves. A pressure field dipole is then created to prevent flow divergence at the front and back edge of the wind farm. The rigid lid approximation allows closed form expressions that deepen our understanding of the wind farm pressure disturbance.

Surprisingly, the GW and RL solutions are qualitatively similar. Both have an upwind-downwind high-low pressure difference. Pressure forces act to smooth out the deceleration of the wind by the farm. They reduce the deceleration over the farm with a favorable pressure gradient and add deceleration zones upwind and downwind with an adverse pressure gradient. They also produce small areas of deflected and accelerated airflow to the left and right of the farm.

In the real atmosphere, the inversion strength is only about $g' = 0.1 \ ms^{-2}$ and the tropospheric stability is about $N = 0.01 s^{-1}$. With these values, air above the turbine layer may still be significantly displaced but the confinement is sufficient that some of the rigid lid characteristics appear (Figs 1,2,4). The stability values need to be an order of magnitude larger however before the rigid lid approximation becomes quantitatively accurate approximation to the full GW results. (see Table 2).

We propose two applications for the RL solutions. First, they provide an approximate way to compute total farm drag from upwind and downwind pressure measurements. Second, they may apply directly to "industrial" wind farm models that use a rigid lid to reduce computational time and complexity.

12. Acknowledgements

I appreciate useful conversations with Brian Gribben, Graham Hawkes, Neil Adams, Xiaoli Guo Larsen, Jake Badger, Jana Fischereit and Idar Barstad. Insightful comments came from Dries Allaerts and James Bleeg.

13. References

Akhtar, N., Geyer, B. and Schrum, C.: Impacts of accelerating deployment of offshore windfarms on near-surface climate, *Sci Rep* **12**, , https://doi.org/10.1038/s41598-022-22868-9, 2022.

Allaerts, D. and Meyers, J.:   Gravity waves and wind-farm efficiency in neutral and stable conditions. *Boundary-Layer.,* **166,** 269–299. https://doi.org/10.1007/s10546-017-0307-5, 2018

Allaerts, D. and Meyers, J.: Sensitivity and feedback of wind-farm-induced gravity waves. *J. Fluid Mech.*, **862,** 990-1028. doi:10.1017/jfm.2018.969, 2019.

Archer, C.L., Vasel-Be-Hagh, A., Yan, C., Wu, S., Pan, Y., Brodie, J.F. and Maguire, A.E.: Review and evaluation of wake loss models for wind energy applications. *Applied Energy*, **226**, 1187-1207, https://doi.org/10.1016/j.apenergy.2018.05.085 , 2018

Bleeg, J., Purcell, M., Ruisi, R. and Traiger, E.: Wind Farm Blockage and the Consequences of Neglecting Its Impact on Energy Production. *Energies* , *11*, 1609. https://doi.org/10.3390/en11061609 , 2018

Fischereit J., Brown, R., Larsén, X., Badger, J. and G. Hawkes, : Review of mesoscale wind farm parametrizations and their applications. *Boundary-layer Meteorol.,* **182**, 175–224, https://doi.org/10.1007/s10546-021-00652-y. , 2021

Gribben, B and G. Hawkes, G.: A potential flow model for wind turbine induction and wind farm Blockage, Internal Report, Fraser-Nash Consultancy , 2019

Hansen, M.O.L. : Aerodynamics of wind turbines, James & James, ISBN-1-902916-06-9 , 2000

Jensen N.O.: A note on wind generator interaction, Technical Report Risoe-M-2411(EN), Risoe-M-2411(EN), Risø National Laboratory, Roskilde. , 1983

Porté-Agel, F., Bastankhah, M. and Shamsoddin, S.: Wind-Turbine and Wind-Farm Flows: A Review. *Boundary-Layer Meteorol.,* **174,** 1–59. https://doi.org/10.1007/s10546-019-00473-0., 2020

Pryor, S. C., Shepherd, T.J., Volker, P.J.H., Hahmann, A.N., and Barthelmie, R.J.: "Wind Theft" from Onshore Wind Turbine Arrays: Sensitivity to Wind Farm Parameterization and Resolution. *Journal of Applied Meteorology and Climatology*, **59**(1), 153-174. https://doi.org/10.1175/JAMC-D-19-0235.1 , 2020

Smith, R.B.: Gravity Wave effects on Wind Farm efficiency. *Wind Energy*, **13**, Issue 5, 449–458. https://doi.org/10.1002/we.366 , 2010

Smith, R. B.: A Linear Theory of Wind Farm Efficiency and Interaction, *Journal of the Atmospheric Sciences*, *79*(7), 2001-
345   2010. https://journals.ametsoc.org/view/journals/atsc/79/7/JAS-D-22-0009.1.xml , 2022

Stevens R. and Meneveau, C.: Flow structure and turbulence in wind farms. *Annual Review of Fluid Mechanics,* **49**(1):311–339. https://doi.org/10.1146/annurev-fluid-010816-060206 , 2017

350   Wu, K.L. and Porté-Agel, F.: Flow Adjustment Inside and Around Large Finite-Size Wind Farms. *Energies*, **10**, 2164; doi:10.3390/en10122164. 2017

14. Tables

Table 1: Parameters of the reference GW model

Parameter	Symbol	Units	Value
Ambient Wind speed	U	ms^{-1}	10
Layer depth	H	m	400
Applied drag force	F	ms^{-2}	0.0007218
Farm Drag	Drag	Nt	17E06
Interface reduced gravity	g'	ms^{-2}	0.1
Tropospheric Stability	N	s^{-1}	0.01
Rayleigh restoring coefficient	C	s^{-1}	0.00033
Farm size	a, b	km	7 by 7
Grid size	dx, dy	km	0.5 by 0.5

355

Table 2: Wind farm disturbance properties as stability is increased towards the rigid lid limit. The value A is the estimated strength of the pressure dipole.

g'	N	Maximum Displacement	Maximum Deficit	Gamma γ	Δp (9)	A (15)
ms^{-2}	s^{-1}	m	ms^{-1}	-	Pa	$Pa \cdot m$
0.1*	0.01*	11.7	0.468	0.0315	2.38	2335
0	0	18	0.445	0.0226	0	N/A
0.05	0	21	0.539	0.0272	1.33	N/A
0.1	0	18	0.589	0.0236	2.57	N/A
0.2 **	0	21.6	0.682	0.0507	7.06	N/A
1	0	1.72	0.307	0.0196	3.94	8302
10	0	0.135	0.32	0.0194	3.24	6821
100	0	0.0132	0.323	0.0194	3.18	6702
1000	0	0.0013	0.323	0.0194	3.18	6691
1E06	0	1.3E-06	0.323	0.0194	3.18	6689
0	0	18	0.445	0.0226	0	0
0	0.005	13.9	0.444	0.0247	0.595	906
0	0.01	11.9	0.432	0.0257	1.09	1754
0	0.02	8.8	0.403	0.0259	1.81	3132
0	0.1	2.4	0.335	0.0222	2.99	6019
0	1	0.25	0.324	0.0197	3.17	6646
0	10	0.025	0.323	0.0195	3.18	6686
0	100	0.0025	0.323	0.0195	3.18	6689
0	1E06	2.5E-07	0.323	0.0194	3.18	6689

360   *Reference GW case, ** $Fr \approx 1$
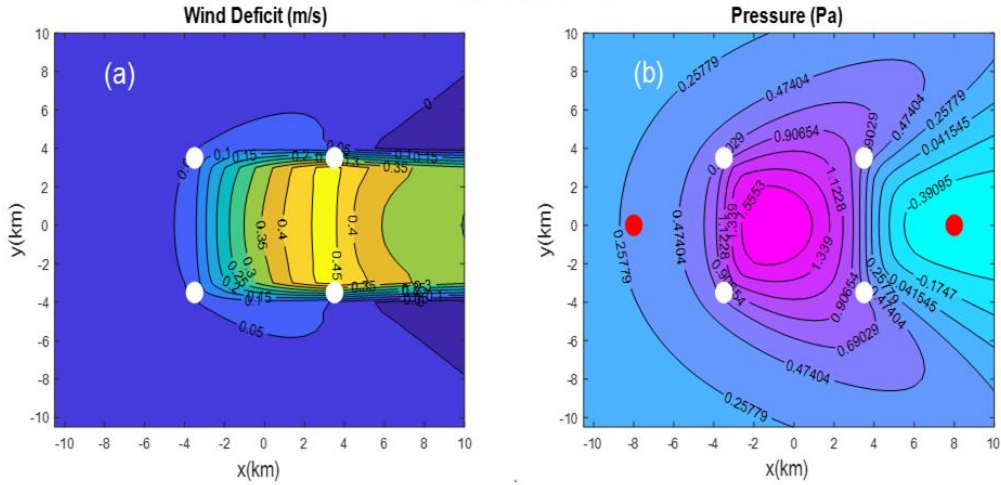
15. Figures

365

Figure 1: Zoom of the disturbance caused by a 7km by 7km wind farm from the realistic gravity wave (GW) model: (a) wind speed deficit (ms^{-1}) and (b) pressure (Pa). Airflow is from left to right. White dots mark the corners of the farm. In (b), the red dots are pressure sampling points. The full domain is 200km by 200km.
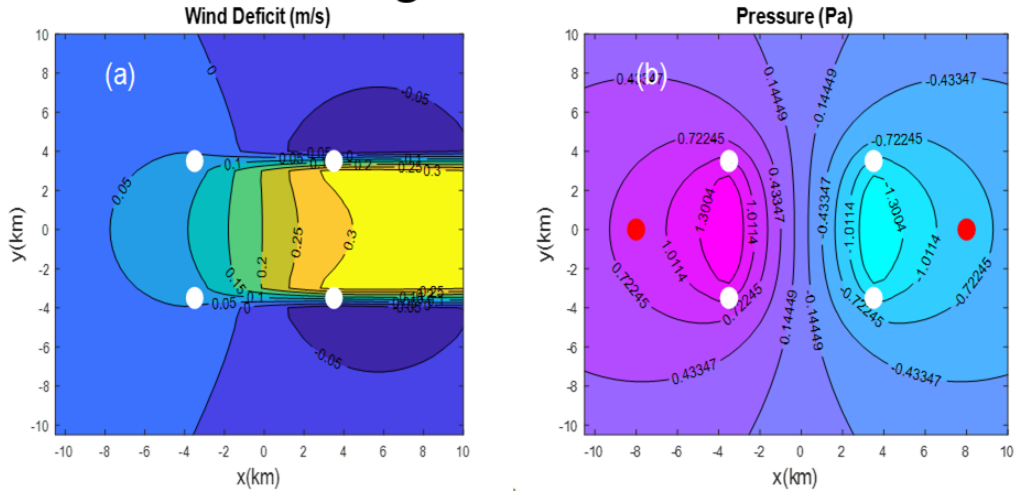
370   Figure 2: Zoom of the disturbance caused by a 7km by 7km wind farm from the idealized rigid lid (RL) case: (a) wind speed deficit (ms^{-1}) and (b) pressure (Pa). Airflow is from left to right. White dots mark the corners of the farm. In (b), the red dots are pressure sampling points. The full domain is 200km by 200km.
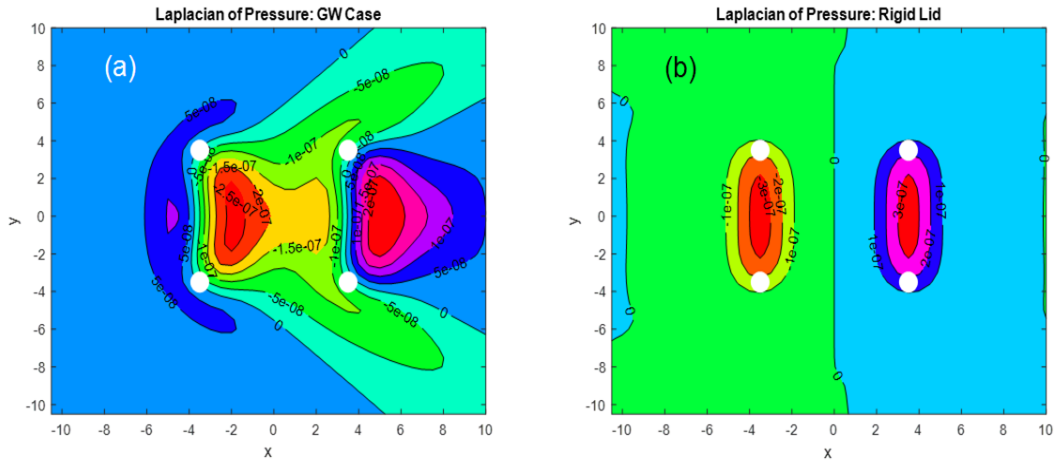
Figure 3: Laplacian of the pressure with units $Pa \cdot m^{-2}$. a) Reference GW case, b) Rigid Lid case. Airflow is from left to
375   right. White dots mark the corners of the farm. A low pass filter has been applied to (b).
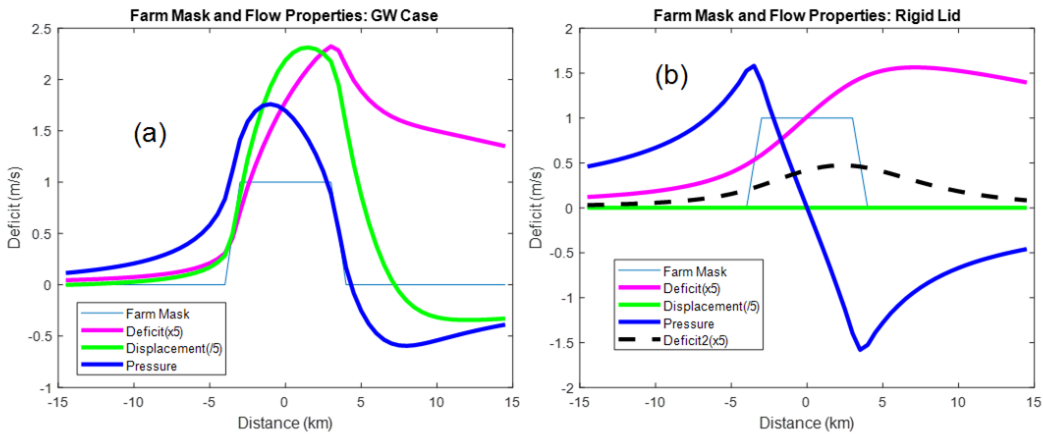
Figure 4: Centerline properties of the farm disturbance including the farm mask, wind speed deficit (x5 m/s), interface displacement (/5 m) and pressure (Pa): a) Reference GW case, b) Rigid Lid case. In (b), the dashed line is the wind speed deficit with a larger Rayleigh restoring coefficient ($C = 0.0033 \ s^{-1}$). The pressure is unchanged. Airflow is from left to right.

380